

Multifunctional Tunable Optical Filter Using MEMS Spatial Light Modulator

Jae-Woong Jeong, *Student Member, IEEE*, Il Woong Jung, *Member, IEEE*, Hee Joon Jung, Douglas M. Baney, *Senior Member, IEEE*, and Olav Solgaard, *Member, IEEE*

Abstract—In this paper, we introduce a multifunctional tunable microelectromechanical systems (MEMS) optical bandpass filter that can continuously and independently tune the center wavelength and the passband spectral width. The filter function is achieved by dispersing the input light on a MEMS spatial light modulator (SLM) that is implemented with gold-coated mirrors microassembled on a MEMS platform. The mirrors are actuated by electrostatic combdrives that are bidirectional and have a maximum stable displacement of 44 μm in both directions for a total range of 88 μm . By actuating the SLM, the 1-dB bandwidth of the filter can be continuously tuned from 0.1 to 1.3 nm, and the 3-dB bandwidth can be tuned from 0.3 to 1.5 nm. In addition, the center wavelength can be fine tuned by actuating the movable blocking mirrors and coarsely tuned over a large spectral range by rotating the grating. [2009-0191]

Index Terms—Microassembly, microelectromechanical systems (MEMS) platform, micromirror, optical bandpass filter, optical communication, tunable filter.

I. INTRODUCTION

WAVELENGTH division multiplexing (WDM) is the dominant technology in large-capacity optical networks [1]. Modern WDM systems place increased importance on tunable optical bandpass filters for dynamic wavelength provisioning. Current dense WDM systems require tunable optical filters with a large center wavelength tuning range and a narrow passband to enhance information capacity and spectral efficiency [2]. The optical bandpass filters should ideally provide independent and continuous tuning of center wavelength and bandwidth with low chromatic dispersion and negligible loss variation within the passband [3]. Such tunable optical filters are needed for multiplexing, demultiplexing, and optical add-drop functioning [4].

There are several methods for implementing tunable optical filters, including acousto-optic tunable filters (AOTFs), fiber Bragg grating filters (FBGFs), thin film filters (TFFs), and optical microelectromechanical system (MEMS) filters.

Manuscript received July 31, 2009; revised November 27, 2009; accepted January 28, 2010. Date of publication April 12, 2010; date of current version June 3, 2010. This work was supported by Agilent Technologies. Subject Editor H. Fujita.

J.-W. Jeong, H. J. Jung, and O. Solgaard are with Stanford University, Stanford, CA 94305 USA (e-mail: jjeong1@stanford.edu; hjjung@stanford.edu; solgaard@stanford.edu).

I. W. Jung is with the Center for Nanoscale Materials, Argonne National Laboratory, Argonne, IL 60439 USA (e-mail: ijung@anl.gov).

D. M. Baney is with the Measurement Research Laboratory, Agilent Technologies, Palo Alto, CA 94304 USA (e-mail: doug_baney@agilent.com).

Digital Object Identifier 10.1109/JMEMS.2010.2043641

AOTFs, FBGFs, and TFFs are commercially available, but they have several weaknesses. For example, AOTFs provide multiple channel selection with very high scan speed (μs), but the isolation between channels is not sufficient [1]. In contrast, FBGFs have low insertion loss and negligible crosstalk between channels, but the narrow tuning range limits their applications [5]. Furthermore, their high sensitivity to temperature is problematic for stable operation in ambient conditions [6]. TFFs also provide low-passband loss and crosstalk [7], but, similarly to AOTFs and FBGFs, they do not offer independent control of the center wavelength and the passband.

Optical MEMS filters are particularly promising alternatives to conventional filter technologies due to their capability for precise and independent tuning of both center wavelength and passband [3], [8]–[11]. When combined with diffraction gratings, optical MEMS filters show negligible chromatic dispersion [12], [13]. Several tunable optical filters using micromirror arrays have been reported [8], [9], but the tuning of their center wavelengths and bandwidths is digitalized and not continuous, as required for precise channel selections. Yu *et al.* [3] introduced a tunable optical bandpass filter that precisely and continuously controls both the optical bandwidth and the center wavelength. However, that filter implementation requires in-plane fabrication of vertical mirrors, and the other optical components (such as gratings and lenses) of the system must be placed off-chip. This feature leads to relatively bulky systems, and the fabrication technology puts limits on aperture size.

In this paper, we introduce a MEMS platform technology that allows large vertical mirrors (450 μm tall) to be microassembled on actuated platforms to enable tunable optical bandpass filters [14]. The fabrication process requires only one mask, and the platform technology enables a compact chip size with large apertures and high-quality optical mirrors with very low scattering losses. In addition, electrostatic combdrive actuators connected to the MEMS platforms provide independent and continuous control of the center wavelength and the optical passband.

This paper is organized follows. In Section II, the principle of the tunable optical filter is presented, together with the design of the MEMS spatial light modulator (SLM). The fabrication process, including the microassembly of the mirrors, is described in Section III. The characterization results of the SLMs are described in Section IV. In Section V, the filter setup and filtering results are shown and discussed. Finally, the conclusions of the work appear in Section VI.

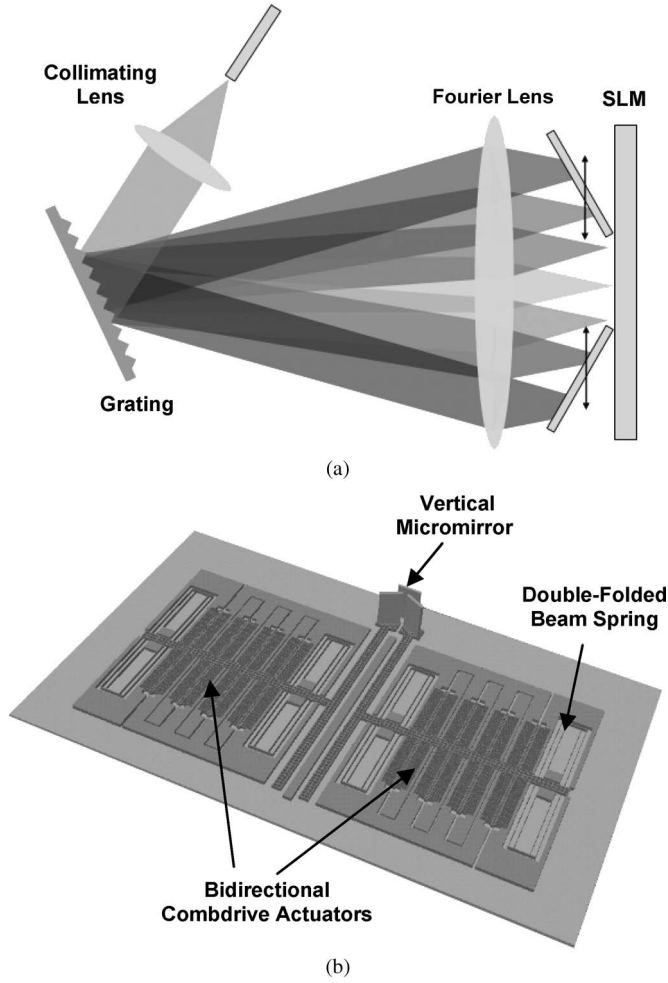


Fig. 1. (a) Operational principle of the MEMS tunable optical bandpass filter. (b) Schematic of the MEMS spatial light modulator.

II. FILTER DESIGN

A. Principle of the Tunable Optical Bandpass Filter and System Design

The principle of the MEMS tunable optical bandpass filter is shown in Fig. 1(a). The tunable optical bandpass filter is based on the dispersion of the incident light by a free-space diffraction grating and the manipulation of the individual spectral components by a MEMS SLM [Fig. 1(b)].

The light from the input/output fiber is collimated and dispersed by the grating, according to the grating angular dispersion relationship of $D_\theta = d\theta/d\lambda = (\sin \theta_i + \sin \theta)/\lambda \cos \theta$, where λ is the light wavelength, and θ_i and θ are the incident and diffraction angles, respectively [15]. The angularly dispersed light is then focused on the MEMS SLM through a Fourier lens. A continuous set of wavelengths reflected from the fixed mirror of the SLM traces back through the system and couples into the input/output fiber. The other wavelengths, which hit the blocking mirrors, are deflected out of the system. By changing the positions of the blocking mirrors independently, therefore, the bandwidth and the center wavelength of the passband can be finely adjusted. To make the extinction ratio high in the rejection band, the blocking mirrors are tilted 30° . The exact value of the blocking-mirror angle is not crit-

ical, but it should be chosen to minimize reflections from the blocking mirrors back into the fiber.

The important parameters of tunable optical filters include insertion loss, bandwidth, channel isolation, and dynamic range. The required specifications depend on the intended applications. In general, WDM networks require filters to have the smallest possible insertion loss, a minimum 3-dB bandwidth of 0.5 nm or less, an extinction ratio better than -20 dB, and a large tuning range to cover the entire C-band. Insertion loss, channel isolation, and tuning range are determined by characteristics of the filter components and the optical setup. To meet the bandwidth requirements, we designed a filter system based on the theoretical analysis of insertion loss described in [3]. According to [3], the shape of a normalized insertion loss profile is determined by the aperture size as adjusted by the relative position of the two blocking mirrors, and it can be expressed as

$$\eta(x_1, x_2, \lambda) = \frac{1}{4} \left| \operatorname{erf} \left(\frac{\sqrt{2}x_1 - \sqrt{2}D_\theta f(\lambda - \lambda_0)}{w} \right) + \operatorname{erf} \left(\frac{-\sqrt{2}x_2 + \sqrt{2}D_\theta f(\lambda - \lambda_0)}{w} \right) \right|^2 \quad (1)$$

where f , w , x_1 , and x_2 are the focal length of lens, the beam waist of the collimated light, and the position of two blocking mirrors. From this equation, the 1- and 3-dB bandwidths are calculated to be $\Delta\lambda_{1\text{-dB}} = [(\Delta x - 1.23w)/D_\theta f]$ and $\Delta\lambda_{3\text{-dB}} = [(\Delta x - 0.55w)/D_\theta f]$, respectively, where Δx indicates the aperture size. Based on these equations, the filter was designed to have minimum 1- and 3-dB bandwidths of 0.1 and 0.3 nm, respectively. The detailed filter system setup and experimental results are illustrated in Section V.

B. SLM Design

The SLM consists of two micromirrors assembled onto actuated MEMS platforms. The out-of-plane vertical mirrors allow the light path to be unhindered by the underlying actuators. Independent control of the positions of the two micromirrors is the key point for tuning both the center wavelength and the bandwidth. To achieve linear and large displacements of the blocking mirrors, we employ bidirectional electrostatic combdrive actuators and double-folded beams (shown in Fig. 2) as springs. The double-folded springs have high stiffness in the direction perpendicular to the actuation direction, thus achieving a larger linear deflection range than single straight-beam springs. The spring constants of the double-folded-beam design in the x - and y -direction are [16]

$$k_x = 2 \times \left[\left(\frac{2Ehb}{L_1} \right)^{-1} + \left(\frac{2Ehb}{L_2} \right)^{-1} \right]^{-1} \quad (2)$$

$$k_y = 2 \times \left[\left(\frac{2Ehb^3}{L_1^3} \right)^{-1} + \left(\frac{2Ehb^3}{L_2^3} \right)^{-1} \right]^{-1} \quad (3)$$

where E is Young's modulus, h is the thickness of the spring, and the geometrical parameters $L_{1,2}$ and b are defined in Fig. 2.

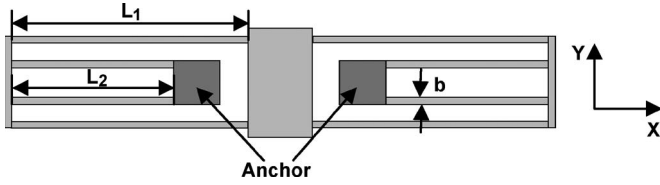


Fig. 2. Design of double-folded-beam spring.

In our design, we chose the following values: $L_1 = 1100 \mu\text{m}$, $L_2 = 920 \mu\text{m}$, $b = 4 \mu\text{m}$, and $h = 40 \mu\text{m}$. Combined with the standard values for Young's modulus for silicon, $E = 169 \text{ GPa}$ [17], this yields spring constants of $k_x = 5.35 \times 10^4 \text{ N/m}$ and $k_y = 0.82 \text{ N/m}$. The folded-beam design achieves a stiffness ratio of

$$\frac{k_x}{k_y} = \left(\frac{L_1^3 + L_2^3}{L_1 + L_2} \right) \frac{1}{b^2} \quad (4)$$

which evaluates to 6.52×10^4 in our design. This high stiffness ratio suppresses unwanted motion in the x -direction, giving the actuator improved stability and larger maximum displacement.

To theoretically model the actuator displacement versus voltage, we used the following equation [18]:

$$\frac{1}{2} V_i^2 \frac{\partial N C_{\text{unit}}}{\partial y} = k_y y \quad (5)$$

where V_i , N , C_{unit} , and k_y are the applied voltage, the number of comb finger pairs, the capacitance of a comb finger pair, and the spring constant described in (3), respectively. The theoretical deflection curve in the quasi-static mode is compared to the experimental data in Section IV.

The maximum stable displacement range is limited by pull-in that can be analyzed using coenergy considerations [19]. Fig. 3 shows the lateral combdrive actuator with six degrees-of-freedom (6-DOF) of motion. These are transversal (x), lateral (y), and piston (z) linear motions and in-plane (φ) and two out-of-plane (θ , ψ) rotational motions. In our design, the suspension is held by four springs at its corners, therefore, φ -rotation is suppressed. Further, the combs are located in one plane, therefore, θ -rotation and z -motion do not short the electrodes and can therefore be neglected. Finally, we see that the combdrives can tolerate large ψ -rotation before shorting occurs, hence, we assume that this failure mode is also insignificant so that the pull-in analysis can be simplified to consider only linear motion in the x - and y -direction.

When the comb gap is large enough, y -direction pull-in is the dominant failure mechanism, thus, it determines the maximum stable displacement range. As we decrease the gap between comb fingers, the driving voltage required for a given displacement is reduced, and at some point, x -direction pull-in, rather than y -direction pull-in, becomes the dominant failure mechanism. In this range of comb gaps, the tradeoff between the maximum stable displacement range and reduction of the driving voltage becomes complex. According to reference [20], the instability increases in proportion to the square of the applied voltage and the inverse cube of the gap between comb fingers. Therefore, in the design of an actuator, it is important to choose a proper combination of the comb gap and the maximum

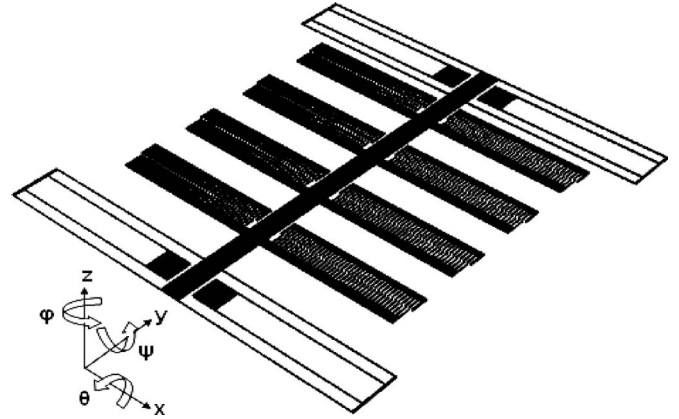


Fig. 3. Schematic of lateral combdrive actuator with 6-DOF shown.

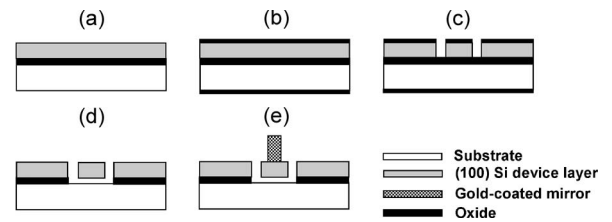


Fig. 4. Fabrication process. (a) SOI wafer. (b) Oxidation. (c) Patterning and DRIE of device layer. (d) Buried oxide etching for release. (e) Micromirror assembly.

driving voltage to achieve a large displacement at a small applied voltage.

Our combdrives are designed to have comb fingers that are $4 \mu\text{m}$ wide, $70 \mu\text{m}$ long, and $40 \mu\text{m}$ high. The gap between the fingers is $6.5 \mu\text{m}$, and the total number of movable combs is 320, equally distributed to eight wings of the suspension with 40 combs for each wing. Following [19], we calculate that y -direction pull-in is the dominant failure mechanism, and that the maximum displacement before pull-in is $58.8 \mu\text{m}$.

It is important that the MEMS platform has the preferred lateral motion as its dominant mode, and that this dominant mode does not couple to other modes. To make sure these conditions are satisfied in the actuator design, simulations are performed using CoventorWare (developed by Coventor Inc.), which is based on 3-D finite-element method. According to the simulation, the preferred lateral motion is the first mode with a resonance frequency of 695.14 Hz and it is well-separated from higher order modes, which are out-of-plane motions at the extremities.

III. FABRICATION PROCESS

The fabrication process is shown in Fig. 4. The MEMS platforms and the micromirrors are fabricated independently on the same silicon-on-insulator (SOI) wafer and combined using microassembly to complete the MEMS SLM. The fabrication process therefore only requires a single mask for defining combdrive actuators and micromirror elements, which makes the process simple and cost effective.

The fabrication starts with a $4''$ SOI wafer that is formed with a $40\text{-}\mu\text{m}$ silicon device layer, a $4\text{-}\mu\text{m}$ buried oxide, and a $400\text{-}\mu\text{m}$ silicon substrate. Initially, a $0.8\text{-}\mu\text{m}$ -thick oxide layer

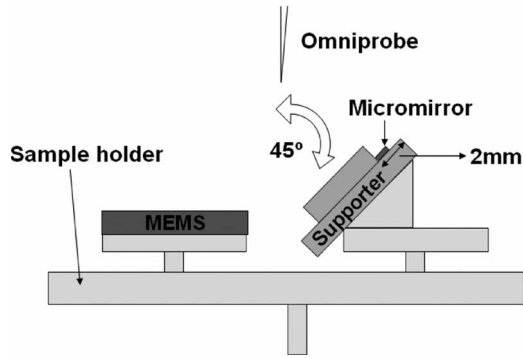


Fig. 5. MEMS platform and mirror preparation for microassembly.

is grown on the wafer by wet oxidation at 1000 °C. This thin oxide layer is used as a hard mask for deep reactive ion etching (DRIE). Following the oxidation, 1 μm of Shipley 3612 photoresist is spun and patterned, and the pattern is etched into the oxide hard mask. The device layer is then etched using DRIE. Before dicing, the wafer is coated with 7 μm of SPR220-7 photoresist for protection. Dicing tape is then attached to the backside of the wafer, and the wafer is sawed into 7.65 mm \times 7.65 mm dies.

To release the devices, individual devices are separated by breaking the wafer along the dicing lines. To remove the resist, each device is soaked sequentially in acetone/methanol/isopropyl alcohol for 20 min/5 min/5 min, respectively. Subsequently, the devices are dipped in 49% liquid hydrofluoric acid to remove the buried oxide under the movable structures. Following this step, devices are rinsed in deionized water and dried in a critical point dryer after soaking in isopropyl alcohol for about 12 h.

The assembly of the mirrors onto the actuator platform is done using a pick-and-place strategy while observing the process under a scanning electron microscope (SEM). Three-dimensional microassembly under SEM monitoring has been studied in the development of object-manipulation technologies such as microrobots [21], microgrippers [22], and electrically charged tools [23]. For the assembly of vertical mirrors, we used an FEI dual-beam focused ion beam (FIB)/SEM equipped with an omniprobe nanomanipulator. This tool, which uses Ga^+ ions accelerated to 30 keV, is capable of nanoscale manipulation of samples, selective deposition of Pt, and site-specific etching of the sample surface with submicrometer precision. Using techniques developed for TEM sample preparation [24], we assembled mirrors measuring 450 μm in height, 311 μm in width, and 40 μm in thickness onto the MEMS platform. Before the assembly, the micromirrors are prepared with a 300-nm-thick gold coating on 5-nm-thick Ti adhesion layer to enhance light reflectivity.

To mount the mirrors vertically, they should be picked by their edges, not their front or back surfaces. This is achieved by preparing the mirrors on a supporter attached to the SEM sample holder at a tilt angle of 45°, while the MEMS chip is flat on the holder, as shown in Fig. 5. By tilting the sample stage through 45°, the vertically standing mirrors can be picked up by the omniprobe by depositing Pt at the connection between the

mirror and omniprobe. After pick-up, the sample stage is tilted back to the initial horizontal position. Then, the mirror is placed in an alignment slot on the MEMS platform, where it is attached permanently by depositing Pt.

To prevent the assembled mirrors from detaching due to high-frequency movements, a 1- μm -thick Pt deposition was made along the large boundary area (400 μm^2) between the mirror and the platform. The Pt deposition over large areas is accelerated by using a high current (3000 pA) Ga^+ ion beam with a large aperture, which is normally utilized for fast etching in the FIB system. The high current (3000 pA) can reduce the total 1- μm -Pt-deposition time for large areas (400 μm^2) by as much as 7–8 h, compared to using low current (30 pA), which is generally used for precise depositions over small areas (1 μm^2). During the FIB process, Ga^+ ion bombardment of the gold-coated surfaces may degrade reflectivity, thus, the ion exposure should be minimized by directing all etching and deposition to the back surface of the mirrors.

The microassembly process is shown in Fig. 6. This microassembly process demonstrates that the FIB/omniprobe enables precise manipulation and assembly and allows relatively large-aperture optical components to be integrated into compact on-chip systems. It is a serial process, however, and is therefore relatively time consuming.

The fixed mirror should be vertical to avoid excessive insertion loss, while the moving mirrors should be vertical so that they can close evenly. Our chosen assembly technique allows the mirrors to be assembled vertically with negligible error. As shown in Fig. 5, the mirror is picked up to be vertical to the MEMS chip and placed in the alignment slot. In this process, the mirror may be tilted slightly. However, the electron beam image gives a high-resolution top view of the MEMS chip, allowing the tilt angle of the mirrors to be finely controlled using the omniprobe. By adjusting the mirrors so that their side walls do not show when observed from the top, we can reduce the mirror tilt to less than 0.01°. In operation, the moving mirrors will, in principle, become slightly tilted because the suspended mirror pads sag a small amount due to the mirror weight, but this effect is negligible in our design.

Fig. 7 shows the fabricated SLM. In contrast to earlier work, in which the mirrors and actuators are fabricated in the same layer [3], the platform technology allows multiple blocking mirrors because the underlying actuators cannot disturb the light path. The platform technology therefore mitigates the maximum displacement limitation of electrostatic MEMS actuators by using multiple blocking mirrors and thereby allow fast and wide center wavelength tuning without having to rotate a bulky grating. However, the maximum number of mirrors will be limited to around eight due to the large area the actuators take in integration.

IV. CHARACTERIZATION OF SLM

The SLM is characterized by measuring both static and dynamic responses. Fig. 8 plots the static deflection curves of the fabricated combdrive actuators in both directions of operation. The measured displacements versus voltage are reasonably well-matched to the theoretical projection given by (5).

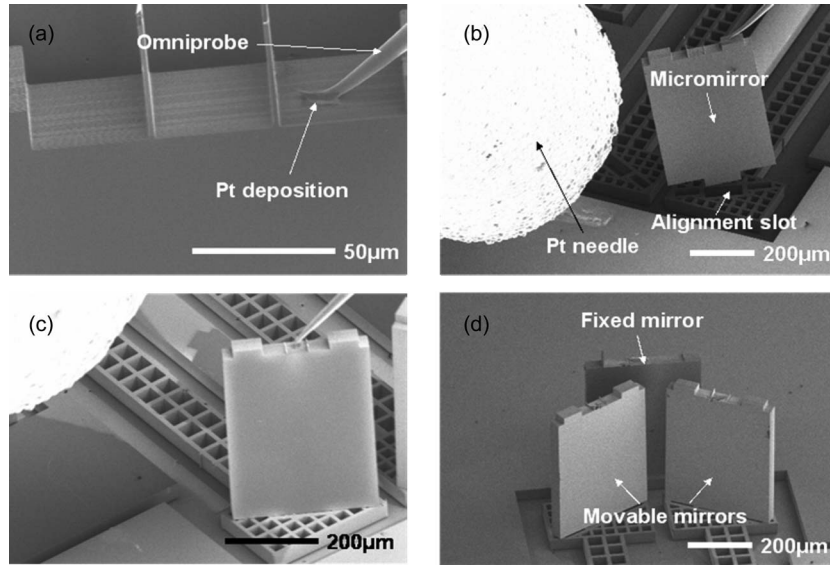


Fig. 6. Microassembly process. (a) Deposit Pt to pick up a micromirror by the omniprobe. (b) Move the mirror to a target spot. (c) Assemble the mirror on the platform and permanently attach it by Pt deposition. (d) Detach the omniprobe.

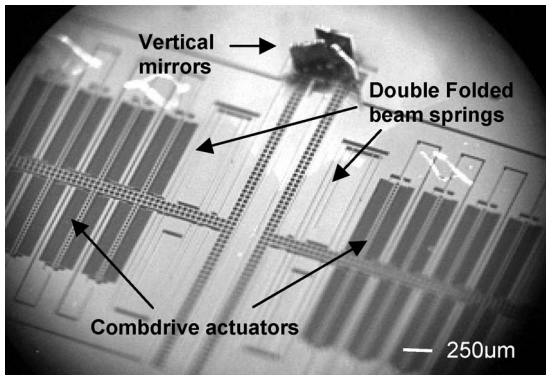


Fig. 7. Microscope image of the fabricated SLM.

(We used a measured spring width of $b \approx 4.1 \mu\text{m}$ in the calculations.) The measurements show that the actuator has a maximum stable displacement of $\sim 44 \mu\text{m}$ in both directions for a total maximum range of $\sim 88 \mu\text{m}$. The failure mode is pull-in in the direction of travel, as predicted by our analysis in Section II, but the measured displacement range is smaller than the theoretically derived value. We believe that the discrepancy is mainly due to fabrication inaccuracies and fringing fields that are not adequately considered in the analytical models. Using two actuated mirrors, the SLM can then control the aperture size over a total range of $176 \mu\text{m}$. In our design, the initial spacing of the two mirror pads is set to $50 \mu\text{m}$, therefore limiting the range of aperture adjustments to $\sim 138 \mu\text{m}$.

The frequency response was acquired by measuring variation of the peak-to-peak received optical power as the oscillating mirror is used to block a photodetector. Fig. 9 shows the resulting dynamic frequency response of the actuator measured with a driving voltage of $(45 + 10 \sin 2\pi ft) \text{ V}$. As simulated by CoventorWare, the actuator has its dominant mode at a frequency of $\sim 700 \text{ Hz}$ with a Q factor of 9.5. According to the modal analysis of Section II, the other modes at higher

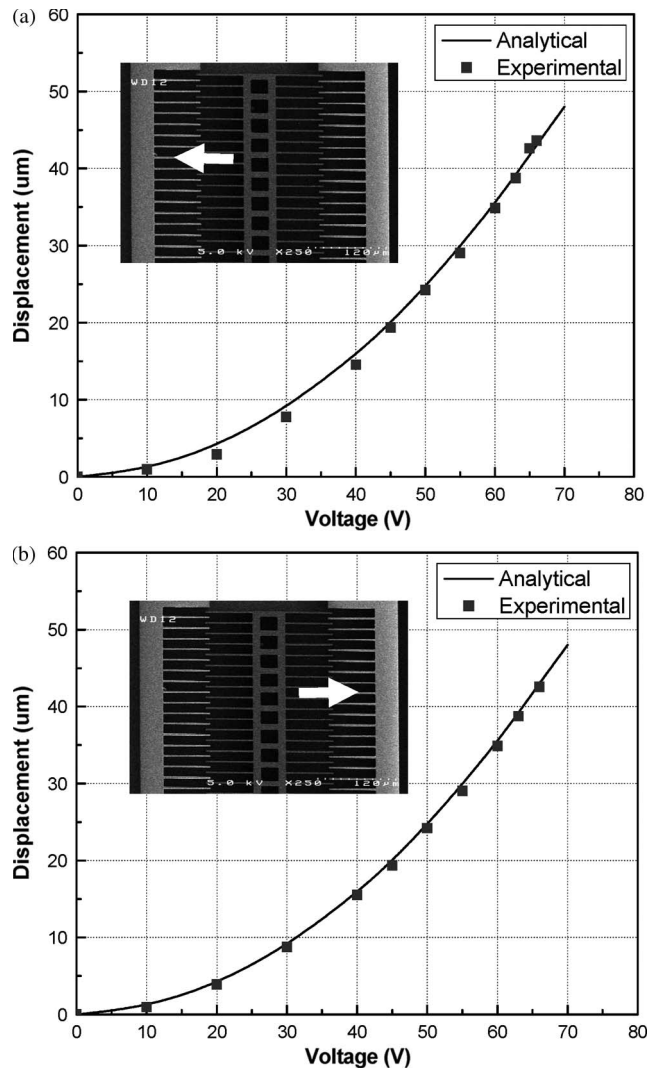


Fig. 8. Static deflection measurement (a) displacement to the left and (b) displacement to the right.

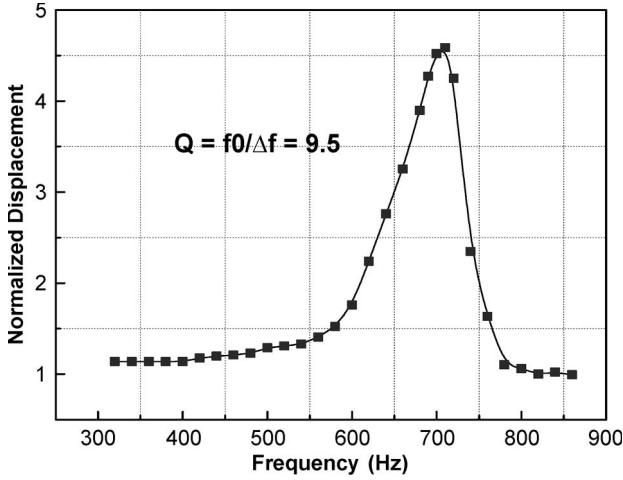


Fig. 9. Dynamic frequency response of the actuator.

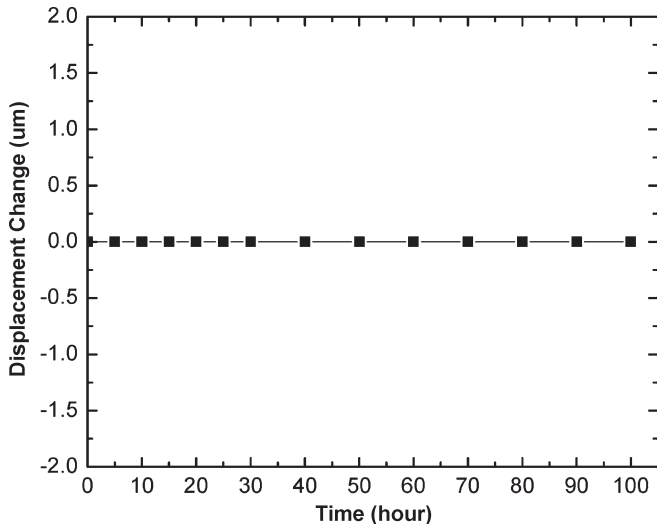


Fig. 10. Displacement variations over 100 h with a constant applied voltage of 55 V.

frequencies do not have lateral motion, so those modes do not cause optical insertion loss variation and cannot be found through the photodetector-blocking measurement.

In operation of the optical filters, it is important that the actuator maintains its position when actuated by a constant voltage. To test the displacement stability over time, we applied 55 V to the actuator and observed its displacement for 100 h (Fig. 10). We found no measurable fluctuations in displacements during this time.

The surface profile of the gold-coated silicon mirrors was investigated, using an optical interferometric profiler (WYKO NT1100, Veeco) to obtain the surface profile, as shown in Fig. 11. The radius of curvature of the mirror is greater than 2 m, and a maximum peak-to-valley deformation of the mirror surface is measured to be 20 nm. The root mean square surface roughness is only ~ 1 nm, which is sufficient for even the most demanding applications in the standard telecommunication bands around $1.55 \mu\text{m}$ wavelength. The measurement shows that the reflectance of the mirror is about 96%.

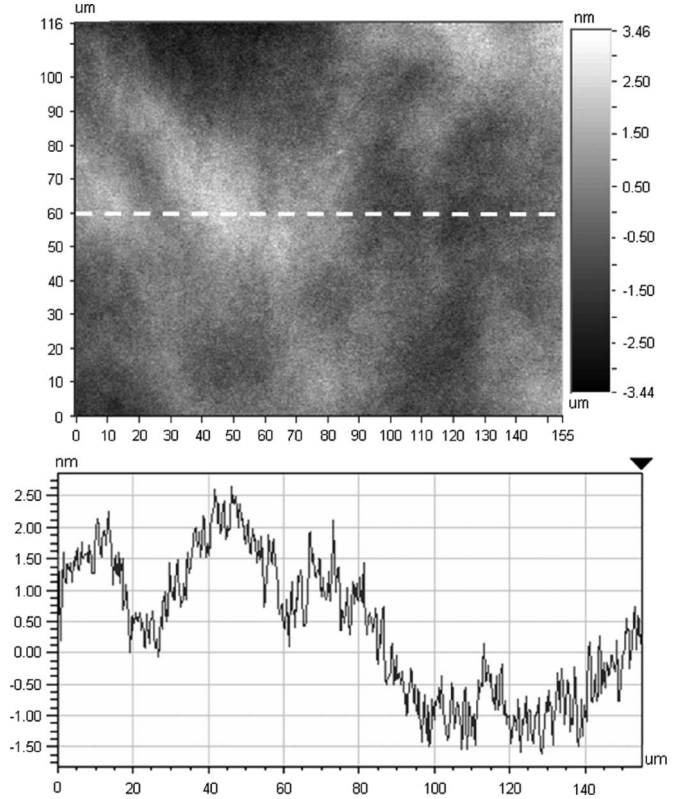


Fig. 11. Interferometric surface profile of the micromirror measured by a WYKO optical surface profiler.

V. FILTER SETUP AND RESULTS

A. Filter Setup

We built a prototype tunable optical bandpass filter by integrating the MEMS SLM with a reflective grating with 900 lines/mm, a fiber beam collimator that yields a ~ 1.76 mm beam diameter, a circulator, and an $f = 20$ mm Fourier lens. The lens we used is a singlet that is designed to balance spherical aberration and diffraction. The size of the beam waist after focusing by the Fourier lens is derived by the modified beam waist formula of $w_0 = (4\lambda f/3\pi w)$, where λ , f , and w are the light wavelength, the focal length of lens, and the beam waist of the collimated light, respectively [25]. This results in a focused beam waist of $15 \mu\text{m}$ at $\lambda = 1550$ nm.

The grating incidence angle θ_i was set to 26° , resulting in a diffraction angle θ_d of 76° at $\lambda = 1550$ nm, as given by the grating equation $d(\sin \theta_i + \sin \theta_d) = m\lambda$, where d is the grating pitch. The angular dispersion at this wavelength is $D_\theta = (\sin \theta_i + \sin \theta) / \lambda \cos \theta = 3.784 \text{ rad}/\mu\text{m}$, and the resulting linear dispersion $D_\theta f$ is $\sim 7.6 \times 10^4$. The midband insertion loss of the filter was ~ -9 dB, partly due to the loss in the fiber connections. The loss in the other components adds up to 8.7 dB and breaks down as follows: circulator (-1.6 dB), collimator (-0.09 dB), Fourier lens (-0.72 dB), grating (-6.08 dB), and SLM (-0.2 dB). The polarization-dependent loss (PDL) of the filter is ~ 7.5 dB and is mainly due to the polarization dependency of the grating. This high PDL can be reduced to below 0.2 dB by using a less polarization-sensitive grating. The maximum extinction outside the passband was limited to

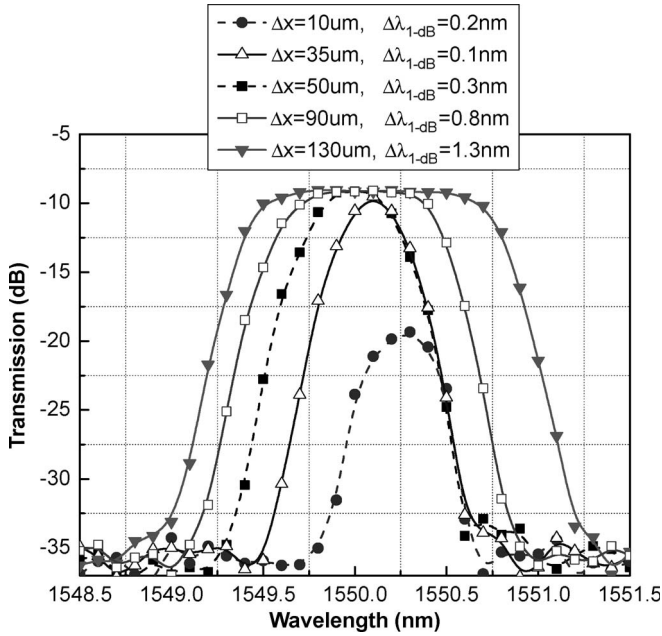


Fig. 12. Measured insertion loss profiles for different MEMS reflector configurations to tune the passband and center wavelength.

~37 dB due to reflections in the fiber collimator. The extinction ratio can be improved by using a lens with an antireflection coating designed for infrared light.

B. Filtering Results and Discussion

Theoretical expressions for insertion loss profile and bandwidths by an optical bandpass filter are demonstrated in Section II. In the following, we use those expressions to calculate the bandwidth, corresponding to a given aperture size, for comparison to measurements.

The insertion loss characteristics for different SLM configurations are demonstrated in Fig. 12. The original aperture (Δx) of 50 μm is varied from 10 to 130 μm by actuating the SLM, leading to a modulation of the 1-dB bandwidth from 0.1 to 1.3 nm and a modulation of the 3-dB bandwidth from 0.3 to 1.5 nm. When attempting to shut off the passband, a 20-dB insertion loss is achieved at an aperture of 10 μm . The measured 1- and 3-dB bandwidths for a 50- μm aperture is 0.3 and 0.5 nm, respectively. These bandwidths are a little smaller than the theoretical values, which are 0.41 and 0.55 nm for the 1- and 3-dB bandwidths, respectively.

The -1 to -20 dB transition band was measured to be 0.45 nm. This spectral width of the transition band is slightly larger than the theoretical value of 0.25 nm based on the expression $1.26w/D_{\theta}f$ [3]. Both the smaller measured bandwidths and larger transition are due to a slightly larger spot size ($w \sim 24 \mu\text{m}$) on the mirrors than the calculated value ($w = 15 \mu\text{m}$). The theoretical insertion loss profile for the aperture size of 50 μm is compared to the measured data in Fig. 13. This plot proves that a smaller focused spot size is required to flatten the passband while reducing the transition band. In optical communications, sharp transition bands lead to

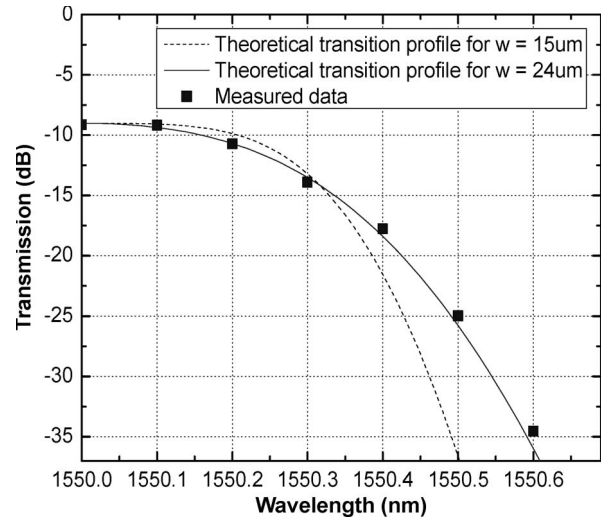


Fig. 13. Comparison between the theoretical and experimental insertion loss profiles.

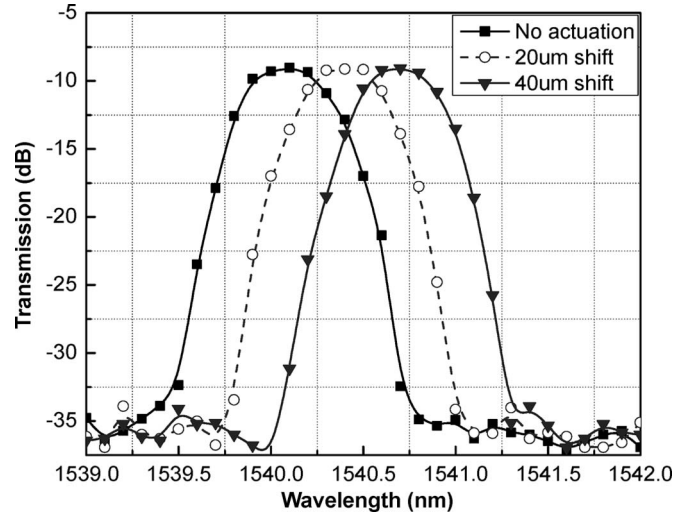


Fig. 14. Measured insertion loss profiles for three different MEMS reflector configurations to shift the center wavelength while maintaining a constant passband.

less amplified spontaneous emission (ASE) noise, and it is thus desired to lower the bit error rate.

Tuning of the center wavelength is important for traffic switching and grooming in network nodes. Our filter can perform precise fine tuning of the center wavelength by moving the mirrors together in the same direction and coarse tuning over large wavelength ranges by varying the incidence angle of the grating. These two tuning principles are shown in Figs. 14 and 15, respectively. By shifting the mirrors 40 μm in the same direction, the center wavelength was tuned 0.6 nm from 1540.1 to 1540.7 nm (Fig. 14). By rotating the grating, the entire C-band could be covered (Fig. 15). Fine tuning can be improved by using an SLM with multiple mirrors for faster tuning over a larger spectral range. In our filter, rotating the grating is manual process, but this method can be improved by a grating integrated on a rotatable MEMS platform.

The experimental results show that our filter satisfies the basic requirements for WDM networks. Its insertion loss is higher

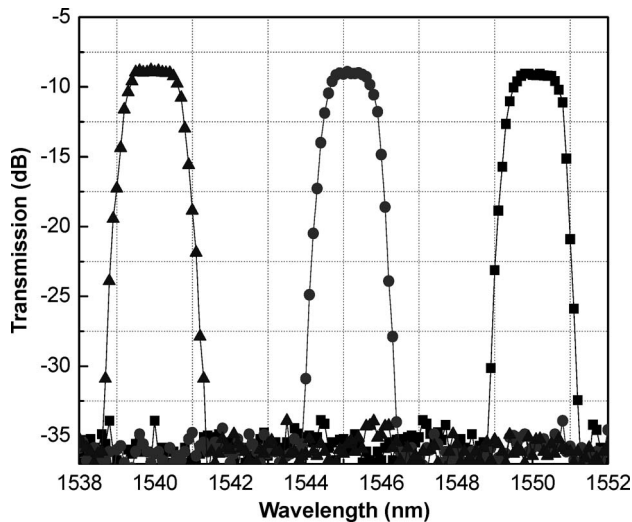


Fig. 15. Measured insertion loss profiles for three different incidence angles on the grating to shift the center wavelength in large steps.

than the loss of other types of filters (e.g., FGBF and AOTF with insertion losses of 0.1 and 4 dB, respectively) [1], but the extinction ratio (over 25 dB) is sufficient to suppress other channels. In addition, the tunability of the 3-dB bandwidth from 0.3 to 1.5 nm not only provides multiple channel selection, but also makes the filter feasible in Telecommunication standardization sector of International Telecommunication Union (ITU-T) WDM grids [26]. Furthermore, separate tuning of the center wavelength and the passband over C-band offers extraordinary flexibility in WDM system design.

VI. CONCLUSION

We have demonstrated a multifunctional MEMS tunable optical bandpass filter that can tune both the center wavelength and the passband independently and continuously. The 1- and 3-dB bandwidths of the filter can be tuned from 0.1 to 1.3 nm and from 0.3 to 1.5 nm, respectively, and the center wavelength can be tuned within the entire C-band. This filter is built based on MEMS platform technology, which offers several advantages. For example, out-of-plane vertical mirrors enable on-chip integration of other optical components such as the grating and lenses to make a compact chip. Since the mirrors are fabricated from the single crystal silicon layer, in addition, the filter maintains high optical quality with minimal scattering loss on the mirror reflection. Furthermore, this configuration can be easily extended to have multiple blocking mirrors (maximum around eight mirrors) for fast tuning over a large spectral range because the light path is never obstructed by underlying actuators. The multifunctionality of this filter is a fascinating feature for optical communications. The tunable filter not only enables dynamic wavelength provisioning as a wavelength selective filter, but also provides improved bit error ratio as an ASE rejection filter by optimizing the signal-to-noise ratio. Therefore, this tunable filter can play a key role in reconfigurable optical add-drop multiplexers, routers, or terminals in the optical network.

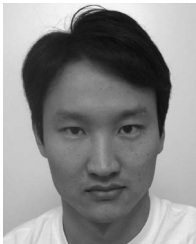
REFERENCES

- [1] D. Sadot and E. Boimovich, "Tunable optical filters for dense WDM networks," *IEEE Commun. Mag.*, vol. 36, no. 12, pp. 50–55, Dec. 1998.
- [2] P. Dittrich, G. Montemezzani, and P. Gunter, "Tunable optical filter for wavelength division multiplexing using dynamic interband photorefractive gratings," *Opt. Commun.*, vol. 214, no. 1–6, pp. 363–370, Dec. 2002.
- [3] K. Yu, D. Lee, N. Park, and O. Solgaard, "Tunable optical bandpass filter with variable-aperture MEMS reflector," *J. Lightw. Technol.*, vol. 24, no. 12, pp. 5095–5102, Dec. 2006.
- [4] C. K. Madsen and J. H. Zhao, *Optical Filter Design and Analysis*. Hoboken, NJ: Wiley, 1999.
- [5] I. C. M. Littler, M. Rochette, and B. J. Eggleton, "Adjustable bandwidth dispersionless bandpass FBG optical filter," *Opt. Express*, vol. 13, no. 9, pp. 3397–3407, May 2005.
- [6] K. Yu, W. Liu, D. Huang, and J. Chang, "C-band three-port tunable bandpass thin film optical filter with low polarization-sensitivity," *Opt. Commun.*, vol. 281, no. 14, pp. 3709–3714, Jul. 2008.
- [7] L. Domash, M. Wu, N. Nemchuk, and E. Ma, "Tunable and switchable multiple-cavity thin film filters," *J. Lightw. Technol.*, vol. 22, no. 1, pp. 126–135, Jan. 2004.
- [8] T. Zhou, D. O. Lopez, M. E. Simon, F. Pardo, V. A. Aksyuk, and D. T. Neilson, "MEMS-based 14 GHz resolution dynamic optical filter," *Electron. Lett.*, vol. 39, no. 24, pp. 1744–1746, Nov. 2003.
- [9] M. Knapczyk, A. Krishnan, L. Grave de Peralta, A. A. Bernussi, and H. Temkin, "Reconfigurable optical filter based on digital mirror arrays," *IEEE Photon. Technol. Lett.*, vol. 17, no. 8, pp. 1743–1745, Aug. 2005.
- [10] G. Wilson, C. J. Chen, P. Gooding, and J. E. Ford, "Spectral filter with independently variable center wavelength and bandwidth," *IEEE Photon. Technol. Lett.*, vol. 18, no. 15, pp. 1660–1662, Aug. 2006.
- [11] K. Yu and N. Park, "Characterization of MEMS optical bandpass filters with narrow transition bands," in *Proc. SPIE—Optical Transmission, Switching, Subsystems III*, Shanghai, China, 2005, vol. 6021, pp. 2R1–2R8.
- [12] J. E. Ford, V. A. Aksyuk, D. J. Bishop, and J. A. Walker, "Wavelength add-drop switching using tilting micromirrors," *J. Lightw. Technol.*, vol. 17, no. 5, pp. 904–911, May 1999.
- [13] T. Sano, T. Iwashima, M. Katayama, T. Kanie, M. Harumoto, M. Shigehara, H. Suganuma, and M. Nishimura, "Novel multichannel tunable chromatic dispersion compensator based on MEMS and diffraction grating," *IEEE Photon. Technol. Lett.*, vol. 15, no. 8, pp. 1109–1110, Aug. 2003.
- [14] J. W. Jeong, I. W. Jung, D. M. Baney, and O. Solgaard, "Tunable optical bandpass filter with high-quality vertical mirrors microassembled on movable MEMS platforms," in *Proc. TRANSDUCERS*, Denver, CO, 2009, pp. 2318–2321.
- [15] E. Hecht, *Optics*. Reading, MA: Addison-Wesley, 2001.
- [16] R. Legtenberg, A. W. Groeneveld, and M. Elwenspoek, "Comb-drive actuators for large displacements," *J. Micromech. Microeng.*, vol. 6, no. 3, pp. 320–329, Sep. 1996.
- [17] K. R. Virwani, A. P. Malshe, W. F. Schmidt, and D. K. Sood, "Young's modulus measurements of silicon nanostructures using a scanning probe system: A non-destructive evaluation approach," *Smart Mater. Struct.*, vol. 12, no. 6, pp. 1028–1032, Dec. 2003.
- [18] C. Liu, *Foundations of MEMS*. Upper Saddle River, NJ: Pearson Edu., Inc., 2006.
- [19] D. Lee and O. Solgaard, "Pull-in analysis of torsional scanners actuated by electrostatic vertical combdrives," *J. Microelectromech. Syst.*, vol. 17, no. 5, pp. 1228–1238, Oct. 2008.
- [20] T. Hirano, T. Furuhashi, K. J. Gabriel, and H. Fujita, "Design, fabrication, and operation of submicron gap comb-drive microactuators," *J. Microelectromech. Syst.*, vol. 1, no. 1, pp. 52–59, Mar. 1992.
- [21] S. Fatikow, J. Seyfried, S. Fahlbusch, A. Bürkle, F. Schmoekel, and H. Woern, "Intelligent microrobotic system for microassembly tasks," in *Proc. 1st Int. Conf. Mechatronics Robot.*, St. Petersburg, Russia, 2000, pp. 22–26.
- [22] A. Cvetanovic, A. Cvetanovic, M. Soucek, D. Andrijasevic, and W. Brenner, "Micro assembly in a SEM chamber and the solution for collision prevention," *Microsyst. Technol.*, vol. 14, no. 6, pp. 835–839, Jun. 2008.
- [23] M. Nakao, K. Tsuchiya, K. Matsumoto, and Y. Hatamura, "Micro handling with rotational needle-type tools under realtime observation," *Ann. CIRP*, vol. 50, no. 1, pp. 9–12, 2001.
- [24] L. Zaykova-Feldman and T. M. Moore, "The total release method for FIB *in-situ* TEM sample preparation," *Microsc. Microanal.*, vol. 11, pp. 848–849, 2005.
- [25] CVI Melles Griot. [Online]. Available: http://www.mellesgriot.com/products/optics/gb_2_3.htm
- [26] *Spectral Grids for WDM Applications*, ITU-T G.694.1, Jun. 2002.



Jae-Woong Jeong (S'09) received the B.S. degree in electrical engineering from the University of Texas, Austin, in 2005, and the M.S. degree in electrical engineering from Stanford University, Stanford, CA, in 2008, where he is currently working toward the Ph.D. degree in electrical engineering.

His research interests include the development of optical MEMS devices and optical systems for applications in imaging and optical communication.



Il Woong Jung (S'01–M'08) received the B.S. and M.S. degrees in physics and applied physics from Yonsei University, Seoul, Korea, in 1997 and 2001, respectively, and the M.S. and Ph.D. degrees in electrical engineering from Stanford University, Stanford, CA, in 2003 and 2007, respectively.

He is currently a Postdoctoral Scholar at the Center for Nanoscale Materials, Argonne National Laboratory, Argonne, IL. His current research interests are in plasmonic nanostructures and MEMS applications for X-rays. His research interests also include

photonic crystal microsystems and optical MEMS devices for applications in sensing and telecommunications, scanning micromirrors, and spatial light modulators for adaptive optics, free-space communication, and imaging applications.



Hee Joon Jung received the dual B.S. degree in metallurgical and ceramic engineering from Yonsei University, Seoul, Korea, in 2005. He is currently working toward the Ph.D. degree in materials science and engineering at Stanford University, Stanford, CA.

His research interests include high-efficiency solar cells with quantum dots and well structures of PbS and thermal analysis of phonon-based materials for heat spreaders with high thermal conductivity by using FIB, TEM, and SThM.



Douglas M. Baney (S'80–M'98–SM'98) received the B.S. degree in electrical engineering from California Polytechnic State University, San Luis Obispo, the M.S. degree in electrical engineering from the University of California, Santa Barbara, and the Ph.D. degree from the Ecole Nationale Supérieure des Telecommunications, Paris, France.

He is a Department Manager in the Measurement Research Laboratory, Agilent Technologies, Palo Alto, CA. He is responsible for applied research in microwave and optical measurement, distributed sensing, and software systems. He joined Hewlett-Packard in 1981 as an R&D engineer, where he designed hybrid GaAs microwave circuits and later optical instrumentation. In 1991, he transferred to the Central Research Laboratory (now within Agilent), where he developed new techniques for optical noise characterization, visible upconversion fiber lasers, nonreciprocal optical components, coherent optical instrumentation, and laser-based optical mice for computers. He has served as a Guest Editor for the JOURNAL OF LIGHTWAVE TECHNOLOGY.

Dr. Baney served as a General Cochair of the Optical Fiber Communications Conference (OFC) and served on the Tyndall Award Selection Committee. He currently serves on the OFC Steering Committee.



Olav Solgaard (S'88–M'90) received the Ph.D. degree from Stanford University, Stanford, CA, in 1992. His doctoral dissertation, "Integrated semiconductor light modulators for fiber-optic and display applications," described, for the first time, deformable grating light valves. These microphotonic devices were the basis for the establishment of a Silicon Valley firm that became Silicon Light Machines (SLM), cofounded by him in 1994.

He served as a consultant to and Technology Advisory Board Member at SLM, which was bought by Cypress Semiconductor Corporation in 2000. From 1992 to 1995, he carried out research on optical MEMS as a Postdoctoral Fellow at the University of California, Berkeley. In 1995, he joined the Faculty of Electrical Engineering, University of California (UC), Davis. His work at UC Davis led to the invention of the multiwavelength fiber-optical switch, which has been developed into commercial products by several companies. In 1999, he joined Stanford University, where he is currently an Associate Professor of electrical engineering. His research interests include optical MEMS, photonic crystals, and atomic force microscopy for applications in telecommunications and biomedicine. He is the author of more than 250 technical publications. He is the holder of 38 patents.

Prof. Solgaard came to Stanford University with the support of a Royal Norwegian Council for Scientific and Industrial Research Fellowship in 1986 and was named a Terman Fellow at Stanford University for the period 1999–2002. He is a Fellow of the Optical Society of America and a member of the Royal Norwegian Society of Sciences and Letters.